2016

930

A149460

AD A149460

R&D CENTER LABORATORY TECHNICAL REPORT

NO. 12957

SCANNING PHOTOACOUSTIC MICROSCOPY OF ALUMINUM WITH ALUMINUM OXIDE, ROUGHNESS STANDARDS AND RUBBER

JUNE 1984

CONTRACT NUMBER DAAE07-81-C-4049

R. L. Thomas, L. D. Favro and P. K. Kuo
Wayne State University
Detroit, MI 48202

and

D. N. Rose, D. Bryk, M. Chaika and J. Patt
US Army Tank-Automotive Command
ATTN: DRSTA-Z
Warren, MI 48090

by

Reproduced From
Best Available Copy

Distribution Unlimited; available for Public Release.

U.S. ARMY TANK-AUTOMOTIVE COMMAND
RESEARCH AND DEVELOPMENT CENTER
Warren, Michigan 48090

20020726142

Unclassified

SECURITY CLASSIFICATION OF THIS PAGE *(When Data Entered)*

REPORT DOCUMENTATION PAGE

READ INSTRUCTIONS BEFORE COMPLETING FORM

1. REPORT NUMBER: 12957	2. GOVT ACCESSION NO.
3. RECIPIENT'S CATALOG NUMBER	
4. TITLE *(and Subtitle)*: Scanning Photoacoustic Microscopy of Aluminum with Aluminum Oxide, Roughness Standards and Rubber	5. TYPE OF REPORT & PERIOD COVERED: Interim Report June 1982-1984
	6. PERFORMING ORG. REPORT NUMBER
7. AUTHOR(s): R. L. Thomas, L. D. Favro, P. K. Kuo, D. N. Rose, D. Bryk, M. Chaika, and J. Patt	8. CONTRACT OR GRANT NUMBER(s): DAAE07-81-C-4049 Modification P00004
9. PERFORMING ORGANIZATION NAME AND ADDRESS: Wayne State University Detroit, MI 48202	10. PROGRAM ELEMENT, PROJECT, TASK AREA & WORK UNIT NUMBERS
11. CONTROLLING OFFICE NAME AND ADDRESS: U.S. Army Research Office P.O. Box 12211 Research Triangle Park, NC 27709	12. REPORT DATE: June, 1984
	13. NUMBER OF PAGES: 52
14. MONITORING AGENCY NAME & ADDRESS*(if different from Controlling Office)*	15. SECURITY CLASS. *(of this report)*
	15a. DECLASSIFICATION/DOWNGRADING SCHEDULE

16. DISTRIBUTION STATEMENT *(of this Report)*

Approved for public release, distribution unlimited.

17. DISTRIBUTION STATEMENT *(of the abstract entered in Block 20, if different from Report)*

18. SUPPLEMENTARY NOTES

The view, opinions, and/or findings contained in this report are those of the author(s) and should not be construed as an official Department of the Army position, policy, or decision, unless so designated by other documentation.

19. KEY WORDS *(Continue on reverse side if necessary and identify by block number)*

Photoacoustic Microscopy, SPAM, Nondestructive Testing, Rubber, Thermal Wave Imaging, Ceramics

20. ABSTRACT *(Continue on reverse side if necessary and identify by block number)*

Thermal wave imaging of coated samples, surface geometries of homogeneous samples, and dispersed particles in rubber samples are presented and discussed. Preliminary results of color-encoding of images are encouraging. Further photothermal (infrared radiation) detection studies of the coated graphite samples are recommended, along with more detailed study of numerical analysis of surface roughness applications. Preparation of rubber samples containing layer defects is also recommended.

DD FORM 1 JAN 73 1473 EDITION OF 1 NOV 65 IS OBSOLETE

Unclassified

SECURITY CLASSIFICATION OF THIS PAGE *(When Data Entered)*

SECURITY CLASSIFICATION OF THIS PAGE(When Data Entered)

SUMMARY

Scanning photoacoustic microscopy (SPAM) and related thermal wave imaging techniques are emerging as methods of non-destructive evaluation (NDE), applicable to surface and near-surface characterization. The usefulness of these methods results from sensitivity to thermal properties, such as diffusivity and boundary conditions, near the point on the surface being probed. Through this sensitivity to localized thermal properties, scanning photoacoustic microscopy can examine beneath the surface of an opaque material for voids, closed or open cracks, and inclusions. The maximum probe depth is approximately 2 mm, and the technique is particularly sensitive to flaws at depths from about 1 micron to 300 microns. SPAM is also well suited to automatic data acquisition.

In this report, thermal wave imaging of coated samples, surface geometries of homogeneous samples, and dispersed particles in rubber samples are discussed. The report also presents thermal wave images which have been sent to TACOM for color encoding.

PREFACE

This work was performed by Wayne State University, Detroit, MI 48202 for the US Army Tank-Automotive Command. Army Research Physicist Douglas Rose of TACOM, Warren, MI, directed the administration of the effort. It was performed at the Department of Physics and Astronomy of Wayne State University with Professor R.L. Thomas as principal investigator, in collaboration with Professor L.D. Favro and Professor P.K. Kuo.

This project was accomplished with funds from the US Army Research Office through Dr. Fred Schmeideshof to TACOM for the establishment of Scanning Photoacoustic Microscopy as a nondestructive evaluation tool and with funds from the Track Elastomer Program through Mr. Jacob Patt of TACOM.

The authors gratefully acknowledge the technical assistance provided by L.J. Inglehart, K.R. Grice, J. Lhota, I. Bergel and Z.J. Feng in the SPAM experiments.

TABLE OF CONTENTS

LIST OF FIGURES

1.0 INTRODUCTION

1.1 Applications. Scanning Photoacoustic Microscopy (SPAM) is an emerging nondestructive evaluation (NDE) technique, initiated at Wayne State University[1], and is applicable to surface and near surface characterization. Research in our laboratory and elsewhere [1-10] is establishing the experimental and theoretical framework for interpreting SPAM micrographs for a variety of subsurface defects. These include a simulated subsurface void[5], delaminations in layered structures[6], closed, lateral subsurface cracks[7,8], and closed slanted cracks.[9] SPAM has also been applied to complex shaped parts such as turbine engine components.[10]

1.2 Technical Principles.

1.2.1 Thermal Wave Generation. Detailed descriptions of SPAM and its potential for nondestructive evaluation (NDE) applications are given in the literature.[1-10] Essentially, the technique may be thought of as thermal wave imaging, where an intensity-modulated and focused laser beam (electron beams or ion beams may also be used) establishes a point source of heat which varies in time at the modulating (or "chopping") frequency. The beam is scanned over the sample surface to generate, one point at a time, a photoacoustic image.

The temperature (T) within the sample, beneath the point on the surface being probed, is a function of time (t) and depth (x). These variations can be modeled by solving the one-dimensional thermal diffusion equation for a semi-infinite solid whose temperature at the boundary is a periodic function of time. Assuming a sinusoidal variation, the steady-state solution is of the form

$$T(x,t) = T_0 \exp[i(qx - \omega t)],$$

where i = square root of - 1 and q, ω, are explained below. The temperature in the solid is periodic in space and time. The space variable is a complex quantity with equal real and imaginary parts, so the thermal wave is very highly damped spatially. Significant temperature variations extend only to one or two multiples of the thermal wavelength. (The thermal wavelength, λ_t , is defined as $2\pi(2k/\omega\rho c)^{1/2}$, where $\omega/2\pi$ = the heat source modulating frequency, and k, ρ , and c are the thermal conductivity, density and heat capacity of the material). The thermal wave accordingly probes only the region close to the surface. The probed depth can be varied experimentally by adjusting the laser (or other heat source) modulation frequency. Typically, the thermal wave depth can be varied from 100 μm to $\sim$2mm. Defects between the surface and that depth are detectable due to variation in thermal properties or discontinuities in thermal properties. Photoacoustic signals are also sensitive to variations in surface conditions, as will be described in the present work.

1.2.2 Thermal Wave Signal Detection Methods. Thermal wave imaging can be performed with any of several thermal wave detection techniques. One method uses a sensitive microphone in conjunction with a gas cell surrounding the point being probed. As the point is alternately heated and cooled, it in turn heats and cools the air (or other gas) in its vicinity, generating an acoustic (sound) signal which the microphone detects. Another technique is optical mirage-effect detection (MIRAGE), whereby a separate laser probe beam is directed parallel to the material surface through the air above the point being probed. The gradient in optical index of refraction of the air, associated with the temperature gradient in the air, causes a deflection of the probe laser beam. This deflection is detected by a position sensor and is the MIRAGE signal.

Thermal wave signals generated by a microphone or probe laser system

have both an amplitude and a phase (relative to the heating laser modulation). Thermal wave images can be generated by recording the amplitude or phase of the signal as a function of position as the relative position between the heating point and the surface of the material under study is scanned.

1.3 Comparison of Methods. A detailed comparison of gas-cell and MIRAGE techniques for detecting slanted cracks has recently been carried out by the Wayne State research group. The results were that MIRAGE detection is especially useful in detecting vertical cracks, and has the advantage of non-contact with the surface being probed. A disadvantage of MIRAGE is that the geometry of the specimen must be such as to allow access by the probe beam, from source to detector, to a line nearly tangent to the surface at all points to be probed. Thermal wave images taken by gas-cell and MIRAGE techniques are presented in this report.

1.4 Data Collection and Processing. These thermal wave scans are controlled by a microprocessor, and digital data acquisition and storage techniques are employed. Most of the data presentations will be in the form of gray scale micrographs. In these micrographs, typically a 6.35 μm x 6.35 μm pixel is used (1 step x 1 step of the x-y stages), resulting in 12,500 to 22,500 points. In some cases, where a larger area is to be scanned, a larger pixel is used. Computer-generated perpective plots have been utilized in some cases. In addition, although gray scale micrographs can be obtained at WSU by intensity-modulating the electron beam of a CRT display, the high-resolution color graphics capability at TACOM was used for most of the micrographs in this report, in order to enhance the display of information generated

by the SPAM process. In some instances (i.e., analysis of the roughness standards data), a microcomputer is used to analyze the data for comparison with conventional measurements of average properties.

In summary, SPAM is applicable for surface and near subsurface NDE, with a depth range which can be varied. The authors have calculated the thermal wave scattering expected theoretically from simple subsurface defects and found excellent agreement with experiments on fabricated defects in uniform materials. Characteristic signatures have been identified which allow these defects to be discriminated from one another. Thermal wave imaging is also well suited to automatic data acquisition.

2.0 THERMAL WAVE IMAGES FOR COLOR ENCODING AT TACOM

2.1 Data Link Between Wayne State and TACOM. In order to circumvent the limited gray scale resolution of the CRT/black and white film display, and to utilize more of the inherent resolution (8 bit) of the data, a digital data transfer link was established between the authors' laboratory at Wayne State University and TACOM. This enables thermal wave images to be transferred in a format which is compatible with the Hewlett-Packard computer system at the Survivability Research Division of the TACOM Tank-Automotive Concepts Laboratory at the Tank-Automotive Command. Images with at least 10,000 points (100 x 100) obtained from several different specimens have been transferred. Included were images of adjacent areas on one specimen to form a 400 x 400 point composite image. In each case, identifiable features are present in the images.

2.2 Images Encoded. A perspective plot and conventional gray scale thermal wave images of four samples are presented in Figs. 1-4.

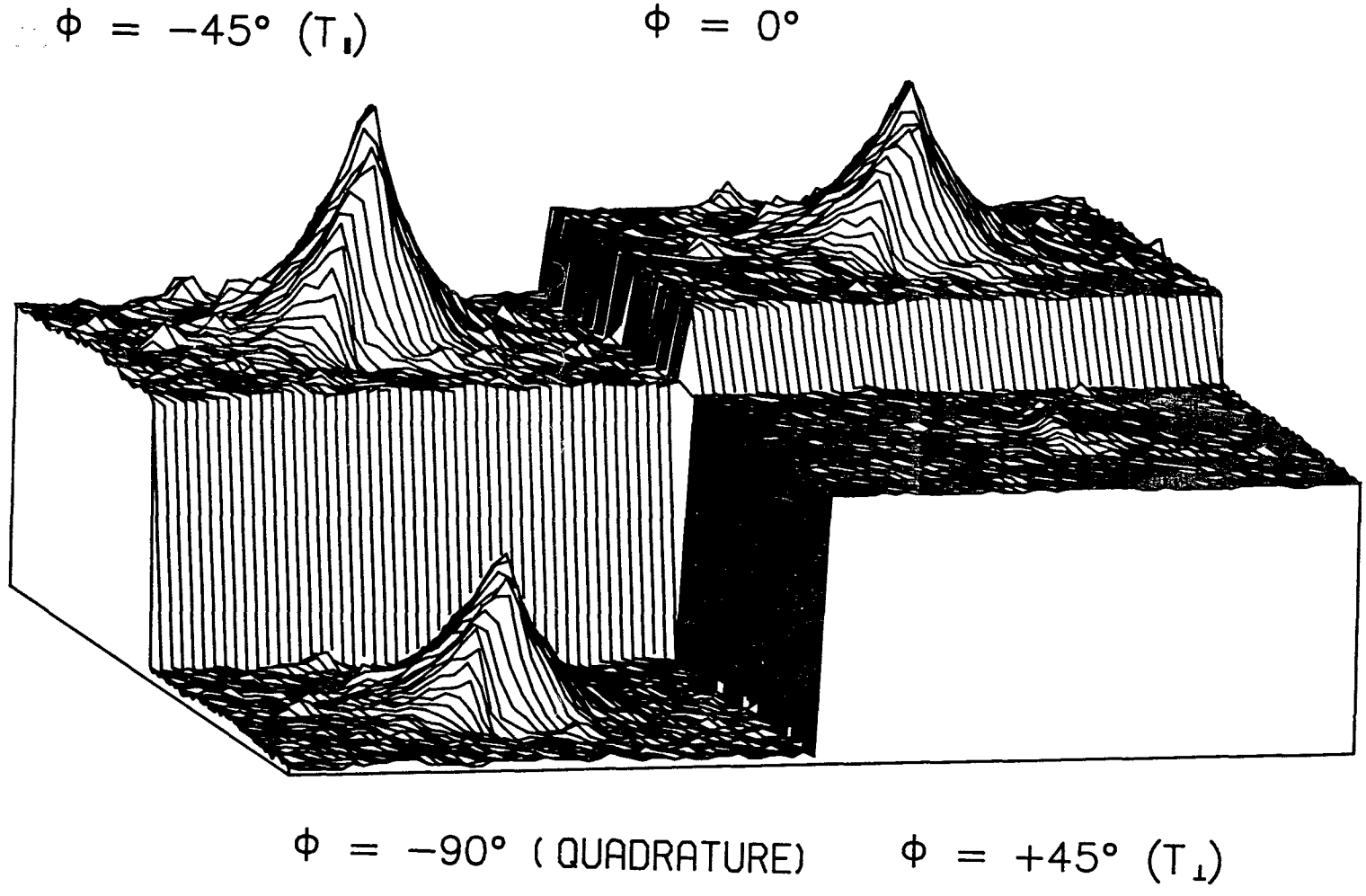

Fig. 1. Photoacoustic microscope (SPAM) thermal wave images of a brittle fracture region beneath a Knoop-indented SiC surface at a frequency of 1 kHz. The four segments of the figure are successive scans of the same region of the sample with four different settings of the phase of the lock-in amplifier. A detailed description is given in Ref. 3.

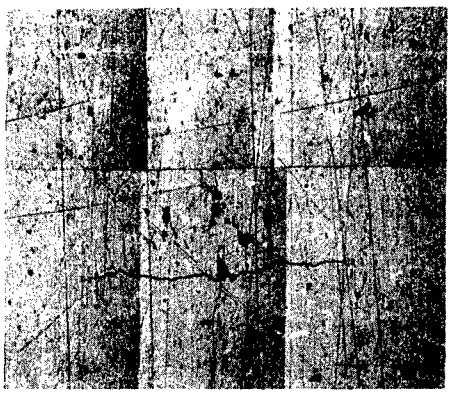

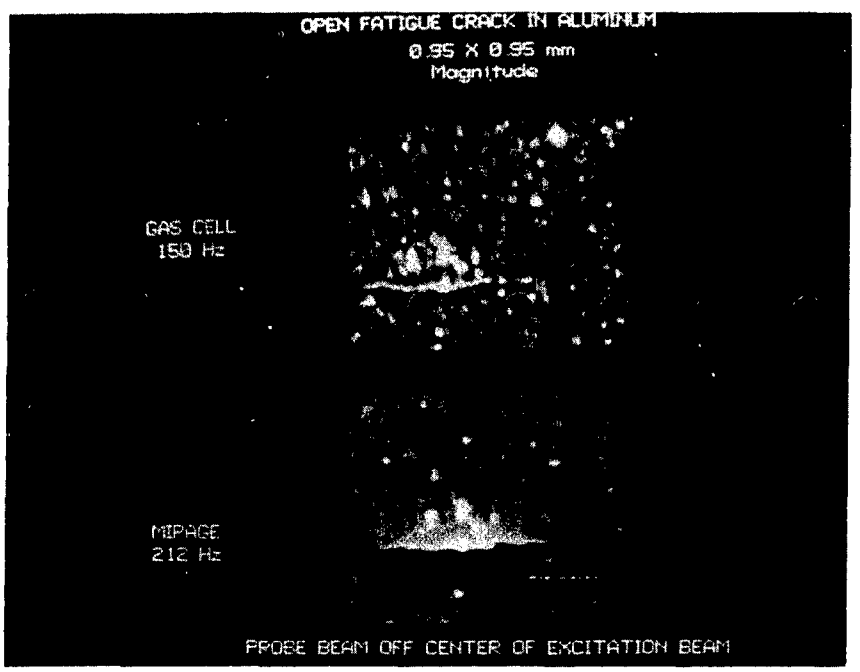

Fig. 2. An optical image (top), Gas-cell thermal wave magnitude (middle), and a MIRAGE thermal wave image (lower) of an open, nearly vertical fatigue crack in an aluminum alloy. A detailed description is given in Ref. 7.

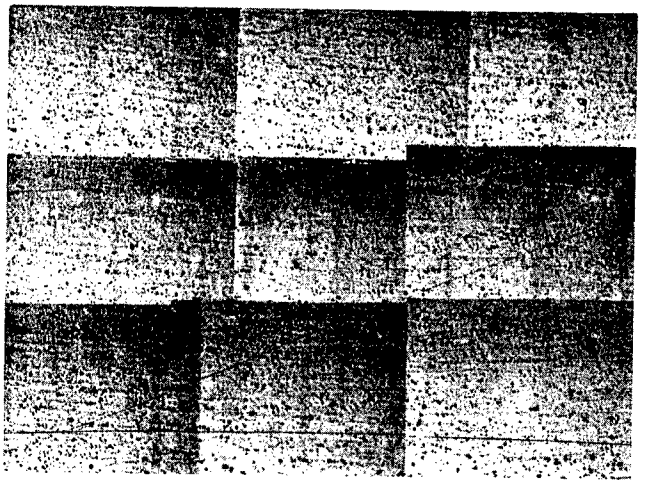

508 μm

a

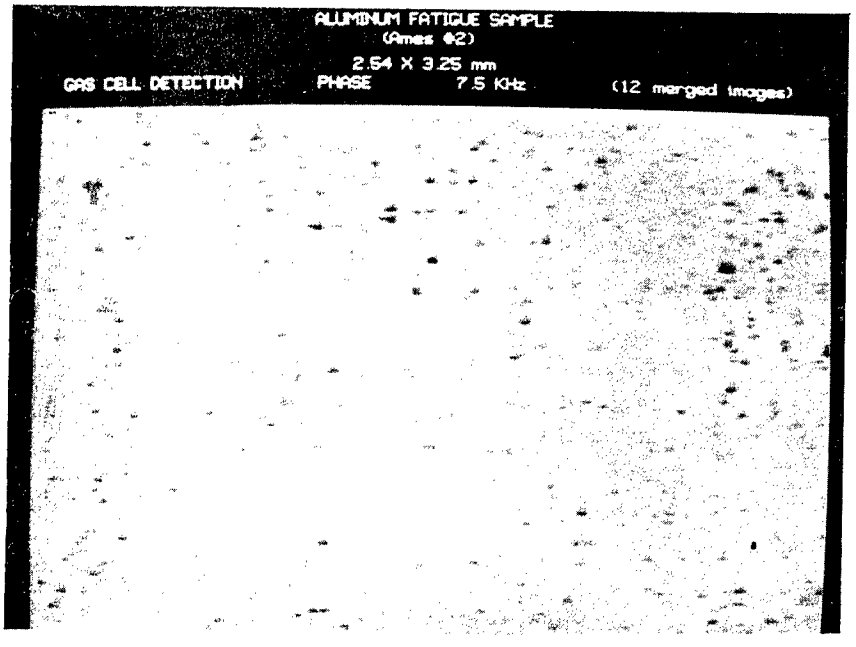

b

Fig. 3. Composite optical and SPAM micrographs of a 400 x 400 point region of an aluminum alloy containing fatigue cracks which are apparently smaller in length than our present detection capability (~ 30μm). A detailed description is given in Ref. 7.

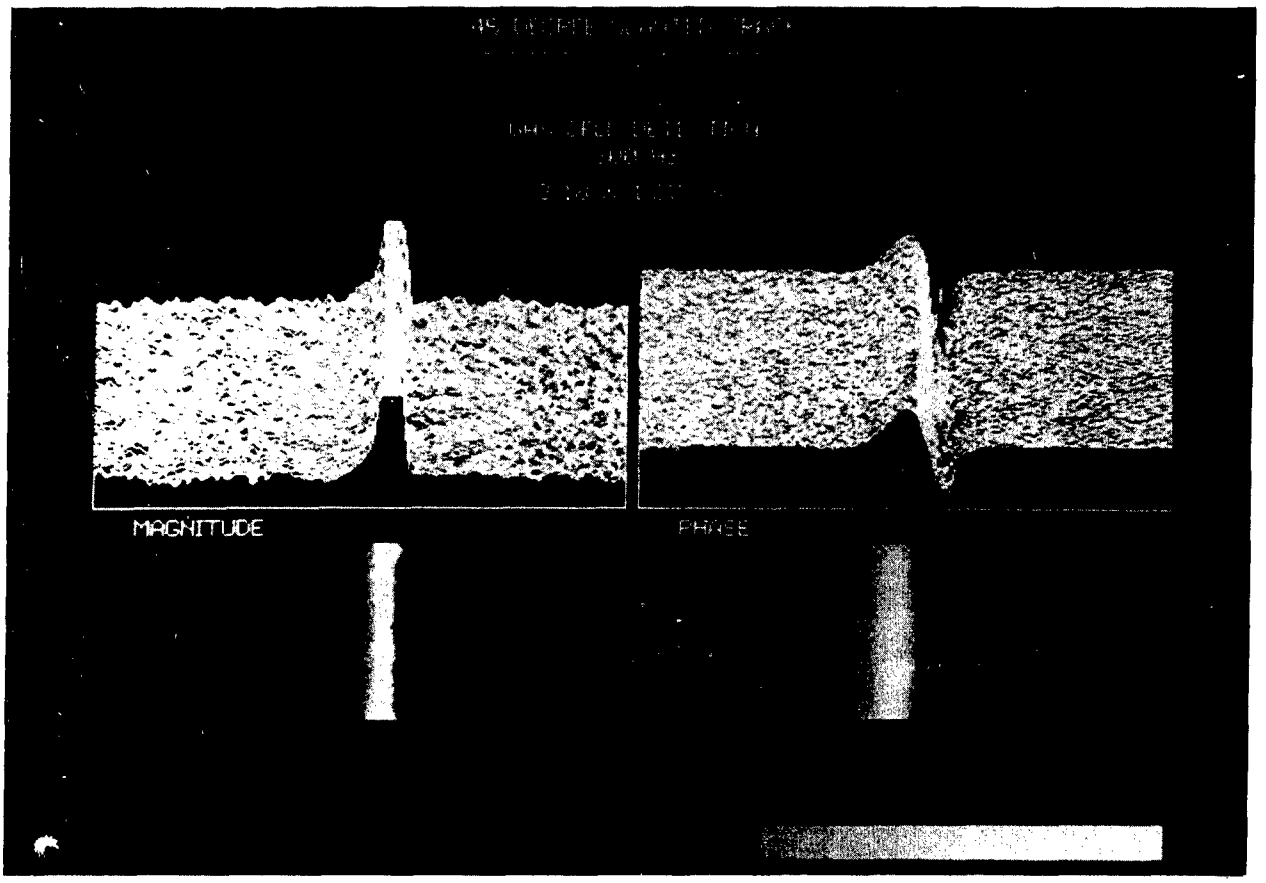

Fig. 4. SPAM magnitude and phase perspective plots (top) and gray scale images (bottom) of a 45^{o} slanted fabricated crack in an aluminum alloy. A detailed description is given in Ref. 9.

Figure 1 shows a four-phase perspective plot[8] of a brittle fracture region beneath a Knoop-indented SiC surface, where gas-cell detection was used. In each of the four separate plots in Fig. 1, the magnitude (height) at a given position represents the component of the photoacoustic signal projected along a phase-vector (phasor) with a given phase relative to the heating laser modulation. Hence, in the - 90 degree plot, the height at each point represents the value of that component of the photoacoustic signal which lags 90 degrees behind that for which the corresponding signal from the undamaged region is maximized.

The authors have demonstrated elsewhere[8] that this characteristic phase dependence is to be expected for thermal wave scattering from a field of closed, lateral cracks which are thermally close to the surface (depth $<< \lambda_t$). These images have also been displayed using the high-resolution color graphics monitor at TACOM.

Figure 2 shows an optical image, two gas-cell thermal wave images (magnitude and phase), and a MIRAGE image of an open, nearly vertical fatigue crack in an aluminum alloy. (Phase image refers to a thermal wave image where changes in phase, rather than of magnitude, of the received signal are recorded). Figure 3 shows optical and gas-cell thermal wave images of another aluminum alloy, both of which are composites of a number of smaller images arranged to illustrate a 400 x 400 point region. This sample has fatigue cracks which are smaller in length than our present detection capability ($\sim$ 30 μm). Color images have been prepared using the same thermal wave data, but the small cracks are still not detectable. Figure 4 illustrates gas-cell magnitude and phase images of a 45 degree slanted fabricated crack in an aluminum alloy, which have been explained theoretically in Reference 9.

3.0 COATED SAMPLES

Specimens of CM 500L coated graphite from San Fernando Laboratories were provided by TACOM to test the ability of thermal wave imaging to assess coating uniformity. Three segments of a 103 mm long sample were provided, with the coating thickness ranging from 98μm at one end to 130μm at the other end. The results of measurements using both SPAM and MIRAGE were negative for the following reasons: With gas-cell detection, the signal change due to variation in the window-to-sample distance during the scan dominates variations attributable to changes in coating thickness. A similar problem is encountered with MIRAGE, where signal variation caused by the varying separation of the probe beam from the surface (due to sample geometry), again, dominates signal variations due to coating thickness variations. In both cases, alignment is critical when one tries to measure very gradual changes in signal. This type of problem is more amenable to photothermal detection, as described by Busse[11]. In this case, the response detected is infrared radiation emitted from the point being probed, which fluctuates at the modulation frequency of the heat source (laser or otherwise). Again, this response has a characteristic magnitude and phase which are influenced by anomalies at depths within range of the thermal wave. Both source (i.e. the point being probed) and detector are effectively points, and the only additional parameter which comes into play is localized surface emissivity.

4.0 SURFACE GEOMETRY

4.1 Samples Studied. Gas-cell and MIRAGE scans were performed on samples with known surface characteristics to study the relationship of the thermal wave signals to surface geometry. Two samples, consisting of simple profiles machined on an aluminum alloy substrate, were studied. In addition, MIRAGE scans were performed on surface roughness standards (Rubert Composite Pocket Set No. 130).

4.2 Step Wedge. The first shape studied is a step wedge, shown in Fig. 5. The step height is 0.4 mm, the maximum wedge width is 1.048mm, and its length is 10.31mm. Figure 6 illustrates two thermal wave images, one of which was obtained using gas-cell detection and the other, the MIRAGE method. The gas-cell image was obtained at 2.5 kHz modulation frequency and a fixed lock-in amplifier phase angle, while the MIRAGE image is a magnitude-only plot (i.e., signal phase relative to heating laser modulation was disregarded) taken at 200 Hz. As one would expect theoretically, the signal has its maximum variation when the heating beam spot is within about one thermal diffusion length of the vertical surface boundary. When the thermal diffusion length in air is very small compared to the step height, there is also an increase (black in Fig. 6) in the MIRAGE signal when the heating beam scans on the wedge, relative to the signal strength obtained from the background surface. This is because the probe beam can pass closer to a heated spot on the wedge than is the case when a point on the background surface is probed. If the modulation frequency is such that the probe beam is several diffusion lengths (in air) above the background surface, a non-zero signal will be possible only when the heating beam is directed on the wedge.

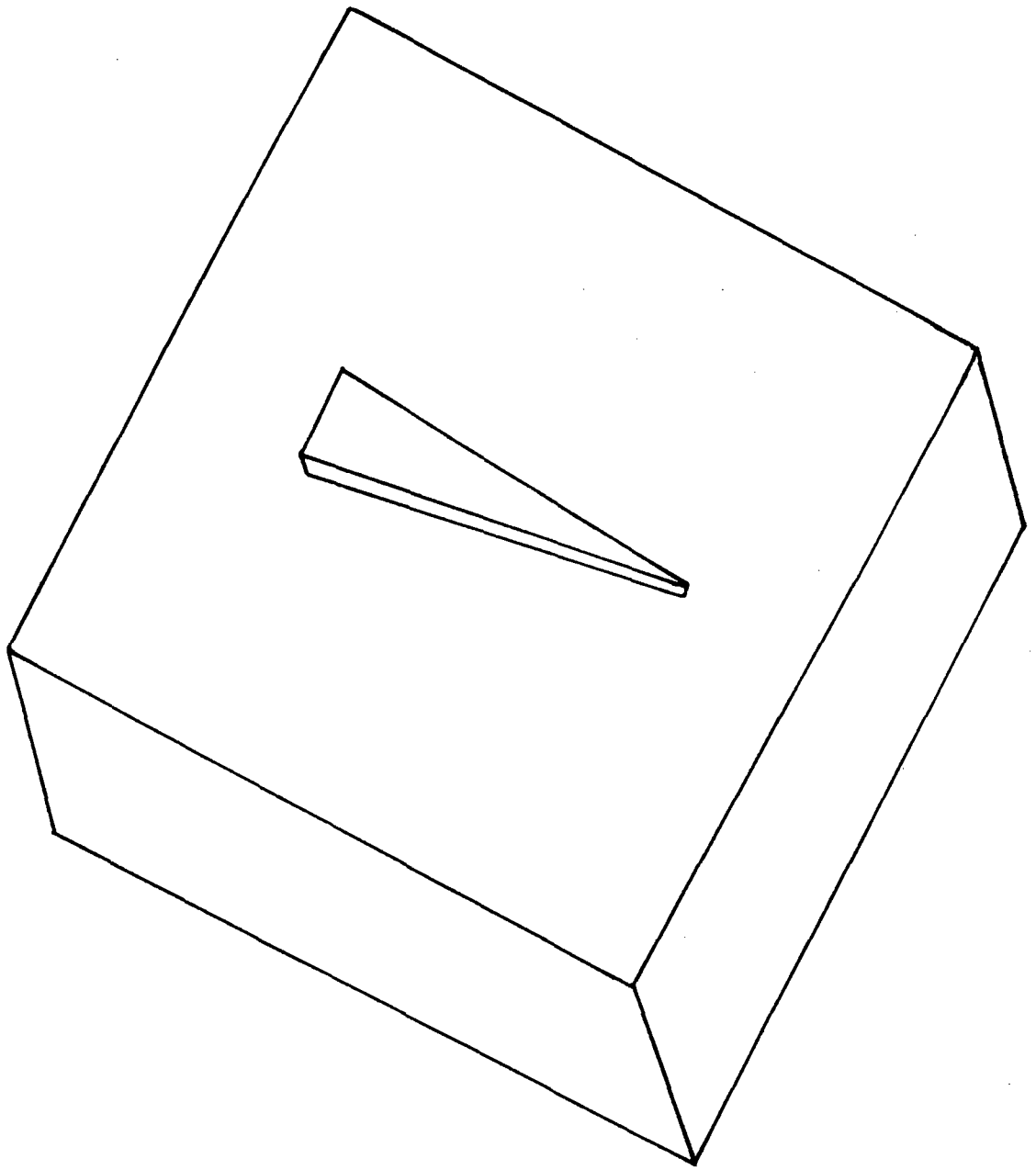

Fig. 5. Schematic drawing of a step wedge on the surface of an aluminum alloy. The step height is 0.4 mm, the maximum wedge width is 1.048mm, and its length is 10.31mm.

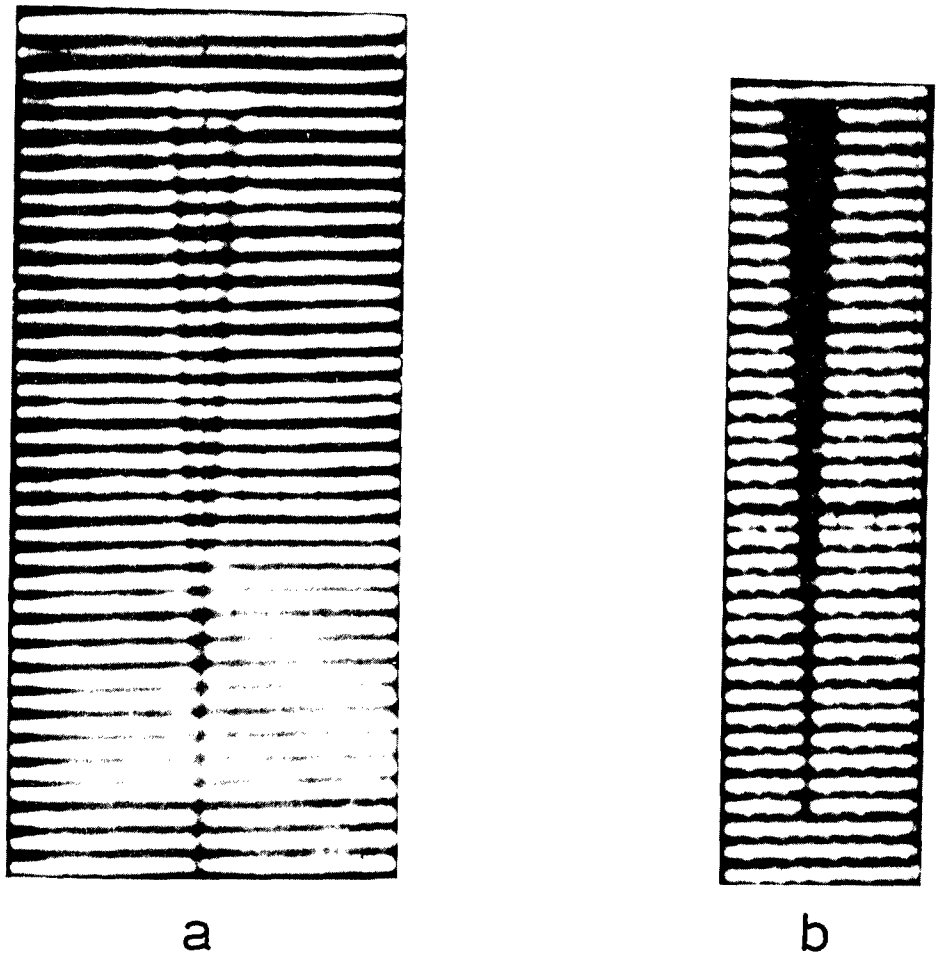

Fig. 6. SPAM thermal wave image at 2.5 kHz and a fixed phase angle (a) and MIRAGE thermal wave magnitude image at 200 Hz (b) for the step wedge shown schematically in Fig. 5. In both images, dark represents a large thermal wave magnitude, and the horizontal lines are an artifact from the scanning.

With gas-cell detection, the predicted and observed signals from points on the central portion of the wedge are essentially identical to those from points on the background surface. Only when the heating beam is within a thermal diffusion length (in the solid) or so of the wedge boundary, are changes in the signal observed. This is because the acoustic signal in a non-resonant gas cell is basically a measure of the integrated surface temperature of the sample, regardless of the heated spot location.

4.3 Parallel Channel Sample. The second surface geometry studied consisted of four equally spaced channels 7.7mm long, 0.43mm wide, 0.43mm deep, with 0.36mm separation, machined with an end mill in an aluminum alloy substrate. A digitally recorded optical image (Fig. 7) was generated by scanning a portion of this surface with an argon ion laser, while monitoring the scattered light with a phototransistor. MIRAGE line scans were then performed, at modulation frequencies from 6.25 Hz to 6.4 kHz. The signal magnitude as a function of position for each of these frequencies is shown in Fig. 8. The signal variations are similar to those for the step wedge, in that the signal undulates as the heating beam repeatedly passes from the top surface, into a channel, and back. As expected, the signal decreases when the heating beam is in a channel and increases when the top surface is probed, since the probe beam can pass closer to the latter than the former.

In studying line scans taken at various modulation frequencies, the data become clearer and better defined with increasing frequency. At 6.25 Hz, the signal variations between top surface and channel are not sharply defined. At 1.6 kHz, 3.2 kHz, and 6.4 kHz, these variations are well defined. At all frequencies, a spike is observed as the heating beam passes from a channel to the top surface, but not when the heating beam enters the next channel. This asymmetry results from the slight anlge between the heating beam and the normal to the surface.

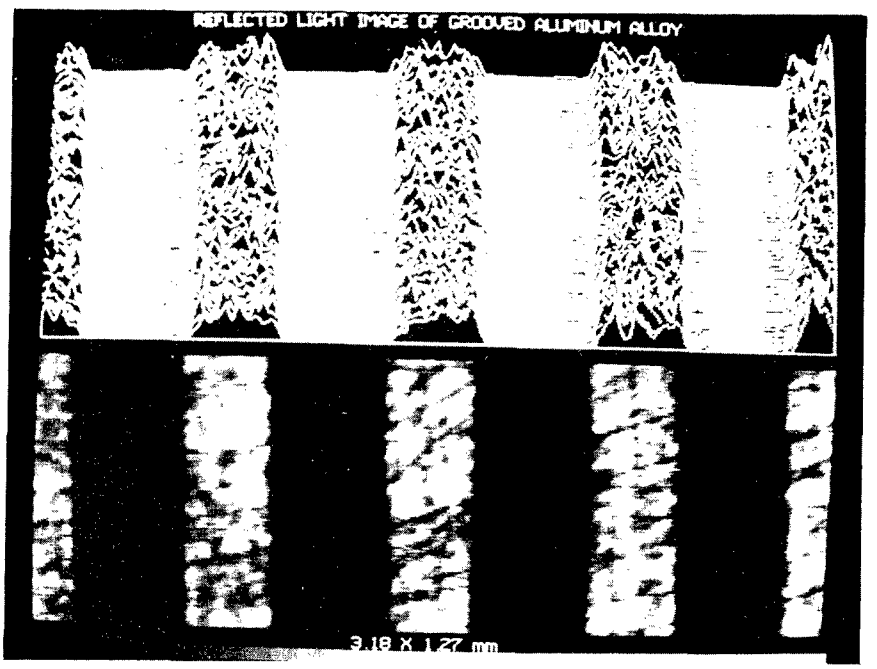

Fig. 7. Digitally recorded optical perspective plot (top) and gray scale image (bottom), using the reflected Ar-ion laser light, of the surface of an aluminum alloy containing four equally spaced channels of dimensions 7.7 mm long, 0.43 mm wide, 0.43 mm deep, and 0.36 mm separation. The dark regions correspond to small reflected intensity.

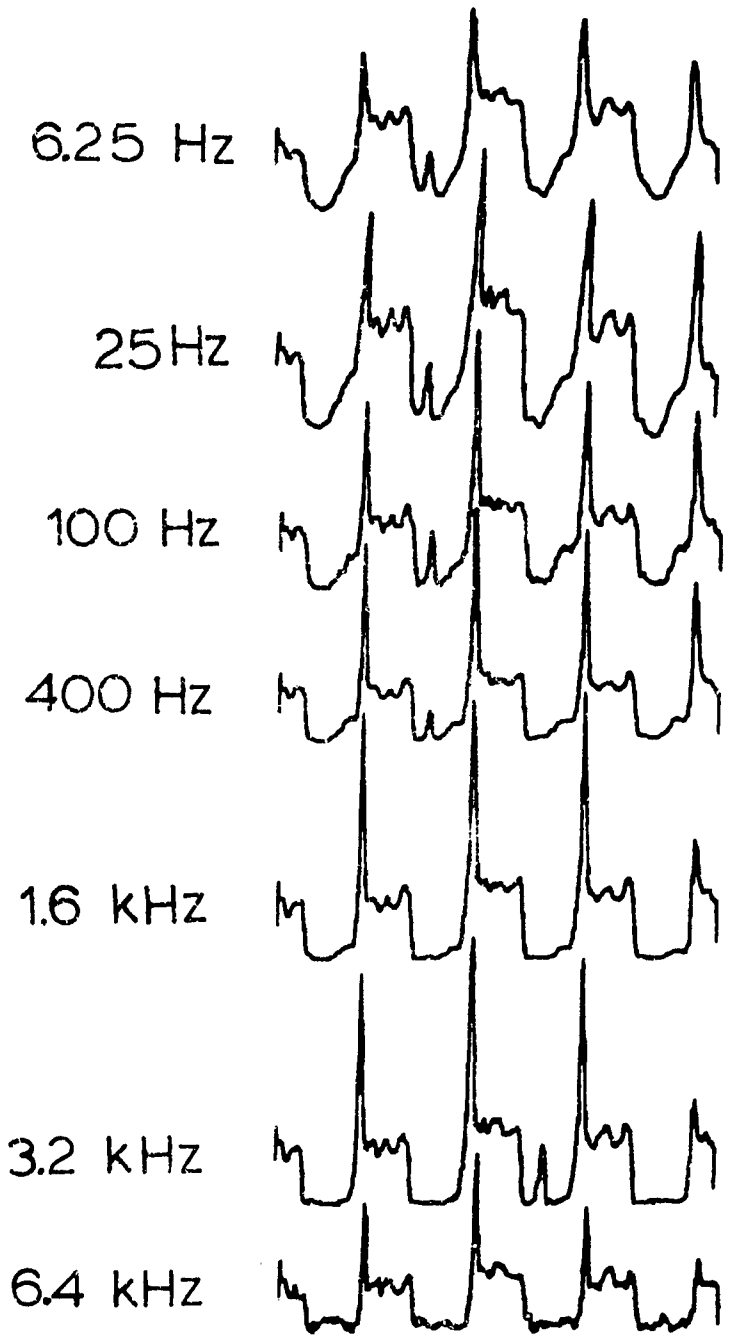

Fig. 8. MIRAGE thermal wave (magnitude) line scans of the aluminum alloy containing four equally spaced channels as a function of frequency (compare with Fig. 7). The length of the scans is 6.35 mm.

4.4 Surface Roughness Standards Samples. The third surface profile on an isotropic substrate was provided by the Rubert Composite Pocket Set No. 130 surface roughness standards. A previous report[12] describes gas-cell measurements performed on these standards. In particular, that report discussed studies of two milling standards, N6 (32 μinches AA) and N7 (63 μinches or 1.6 microns AA). The preliminary assessment was that the RMS photoacoustic phase variation, while giving fair correlation with the nominal surface roughnesses, are likely to depend in a complicated way on the ratio of thermal wavelength to average roughness dimension. It is therefore difficult to extract reliable quantitative roughness information from these signals. As an example of the difficulties involved, this current report has pointed out that, with the step wedge geometry sample, only the edges are easily detected by gas-cell SPAM.

In the present study, a series of line scans were performed on milling standards N6, N7, N8 (125 μinches or 3.175 microns AA) and N9 (250 μinches or 6.35 microns AA), using MIRAGE detection and magnitude-only signal plotting. Line traces for these scans are shown in Figs. 9-12. An Apple II computer program[12] which determines the percentage variation in the signal (RMS variation in proportion to the mean signal) was modified slightly and run for each sample. Because background variations were comparable to or somewhat larger than the roughness-caused signal variations, the curves were divided into five segments, with RMS deviation calculated relative to the best linear fit to each segment. The mean of these five values was then defined to be the rms variation of the entire line, and was divided by the mean of the linear fits to determine the percentage variation. The results for vertical milling standards N6 throuh N9 are shown in Table 1.

Table 1. Comparison of Surface Roughness and MIRAGE Variations.

SAMPLE	MECHANICAL ROUGHNESS (AA) (μ inches)	(microns)	MIRAGE VARIATION (% Magnitude)
N6	32	0.81	5.08 ± 0.69
N7	63	1.6	6.82 ± 1.12
N8	125	3.175	7.24 ± 0.56
N9	250	6.35	46.25 ± 8.5

One can see from the traces in Figs. 9-12, that the ridges increase in height and become more widely spaced as roughness increases. From the data in Table 1 the mechanical roughness increases by a factor of 7.8 from N6 to N9, while the MIRAGE variation increases by a factor of 9.1. Hence there is a fair correlation between mechanical roughnesss and MIRAGE signal variation, as one might expect from MIRAGE studies on the simpler surface geometries previously discussed in this section.

Because the Series N milling roughness standards have non-random surfaces, the authors have also carried out a fast Fourier transform of the MIRAGE scans. The power spectra of the Fourier transforms for three traces of sample N8 are shown in Fig. 13. Recommendations concerning application of this information to characterizing surface roughness are given below in Section 6.

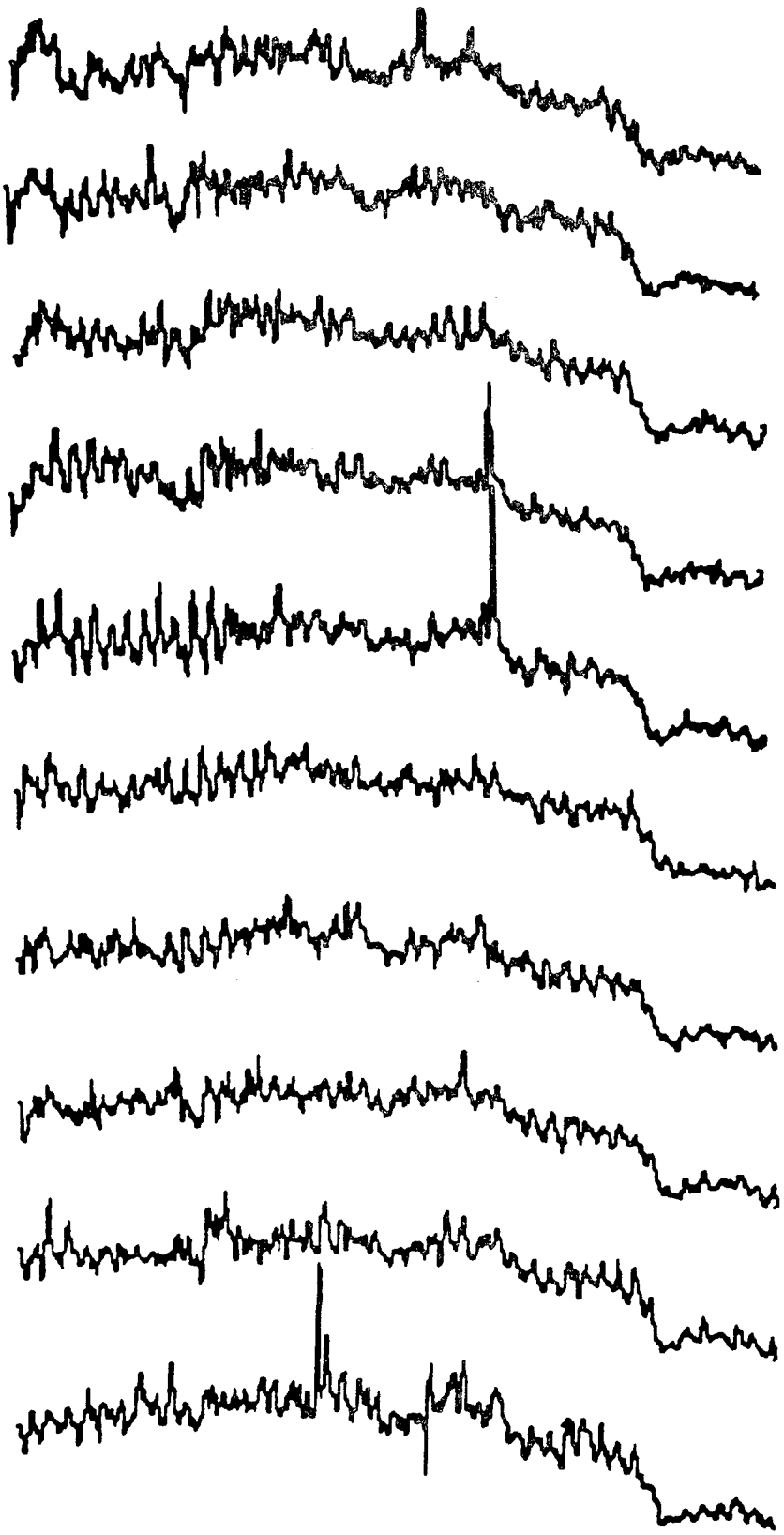

Fig. 9. MIRAGE thermal wave (magnitude) line scans at equally spaced intervals and a frequency of 400 Hz for vertical milling standard N6. The length of the scans is 6.35 mm.

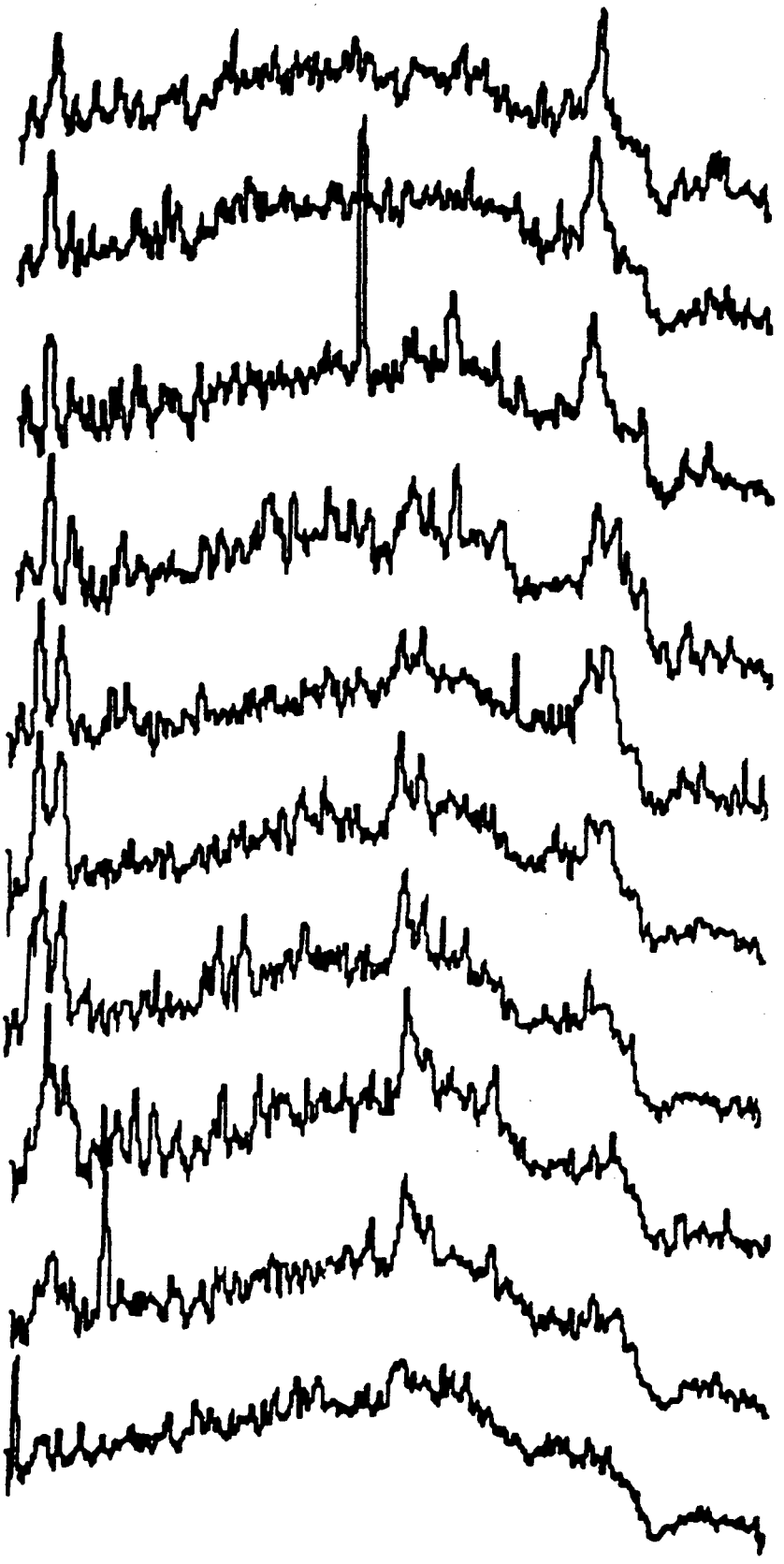

Fig. 10. MIRAGE thermal wave (magnitude) line scans at equally spaced intervals and a frequency of 400 Hz for vertical milling standard N7. The length of the scans is 6.35 mm.

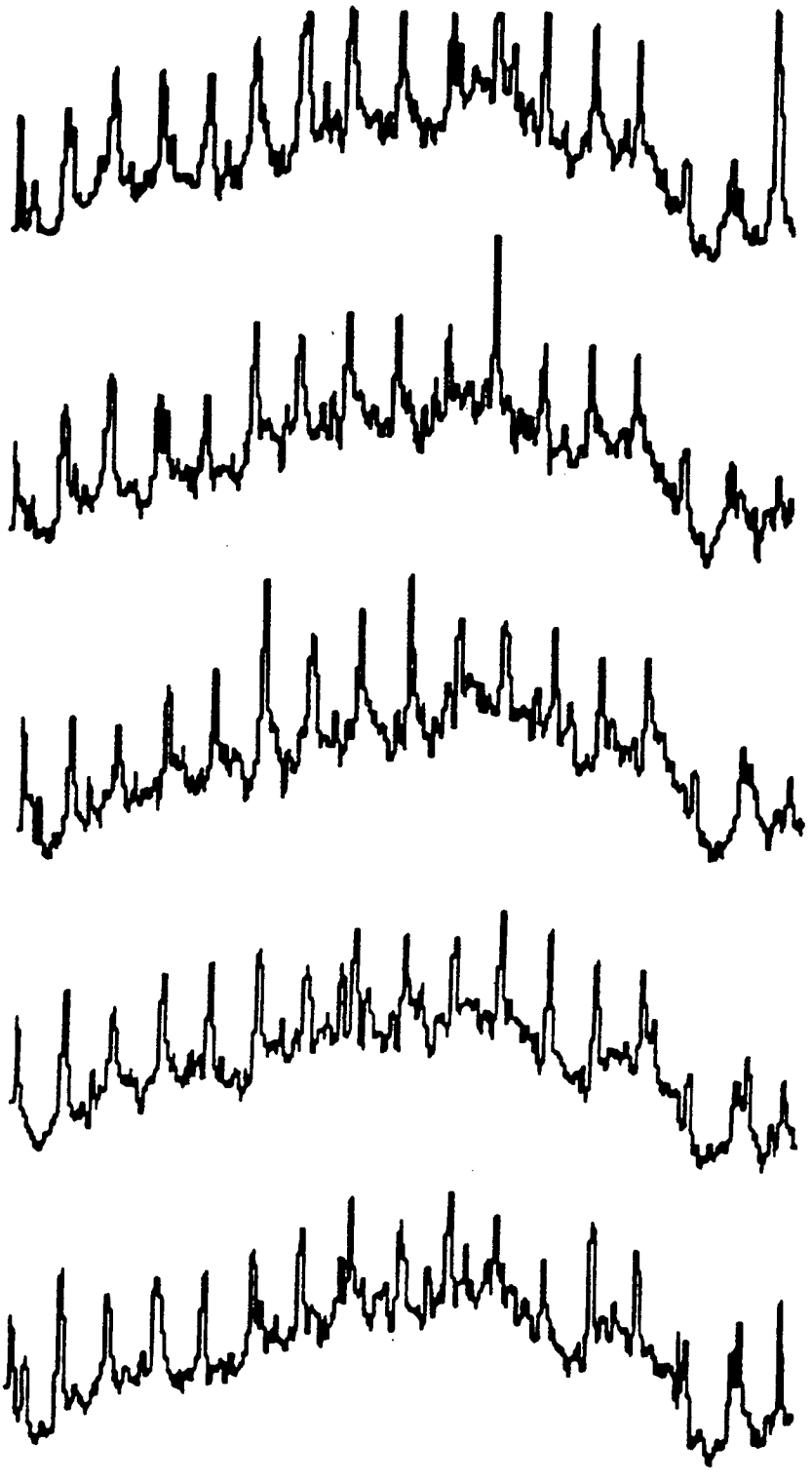

Fig. 11. MIRAGE thermal wave (magnitude) line scans at equally spaced intervals and a frequency of 400 Hz for vertical milling standard N8. The length of the scans is 6.35 mm.

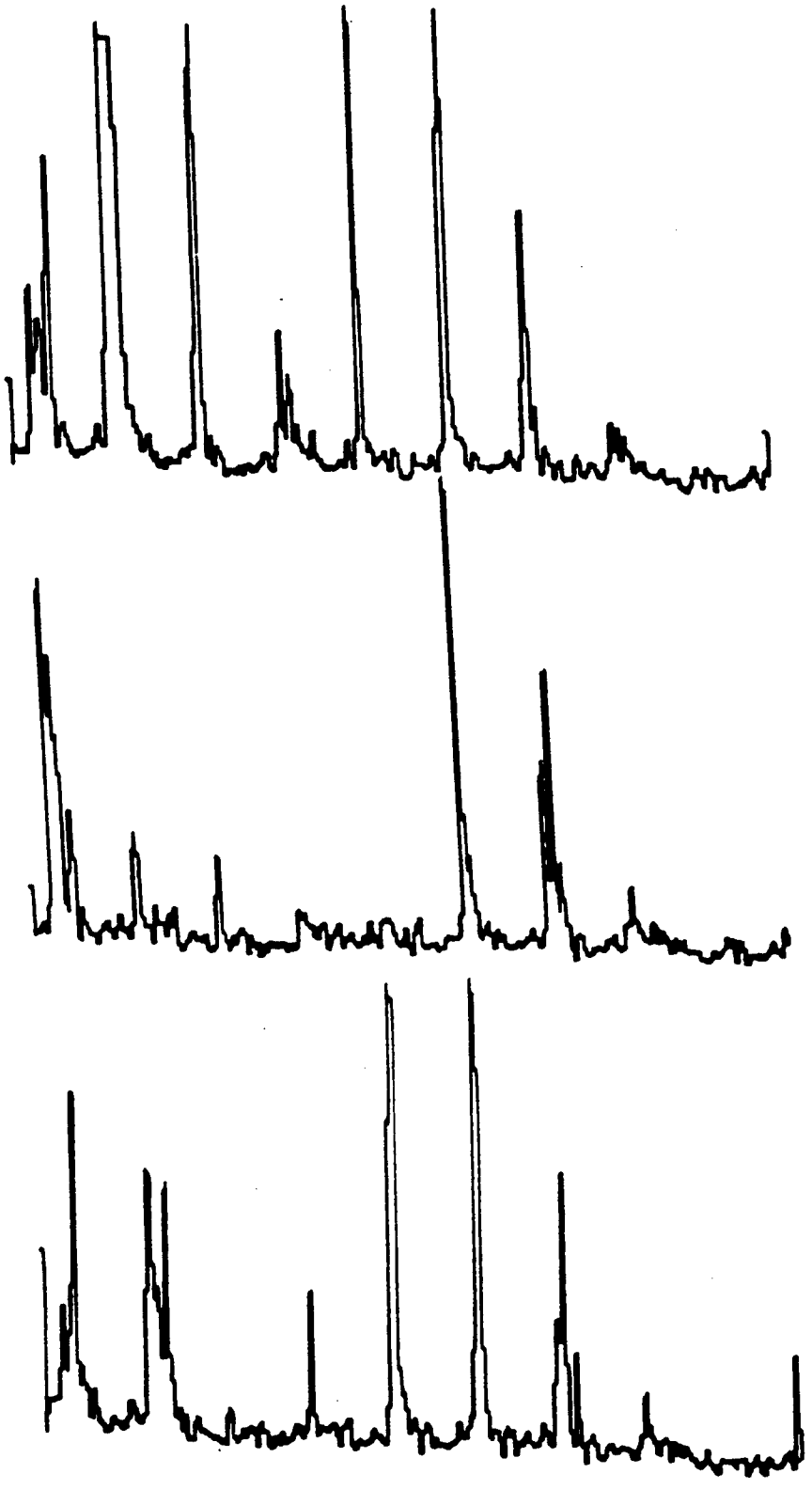

Fig. 12. MIRAGE thermal wave (magnitude) line scans at equally spaced intervals and a frequency of 400 Hz for vertical milling standard N9. The length of the scans is 6.35 mm.

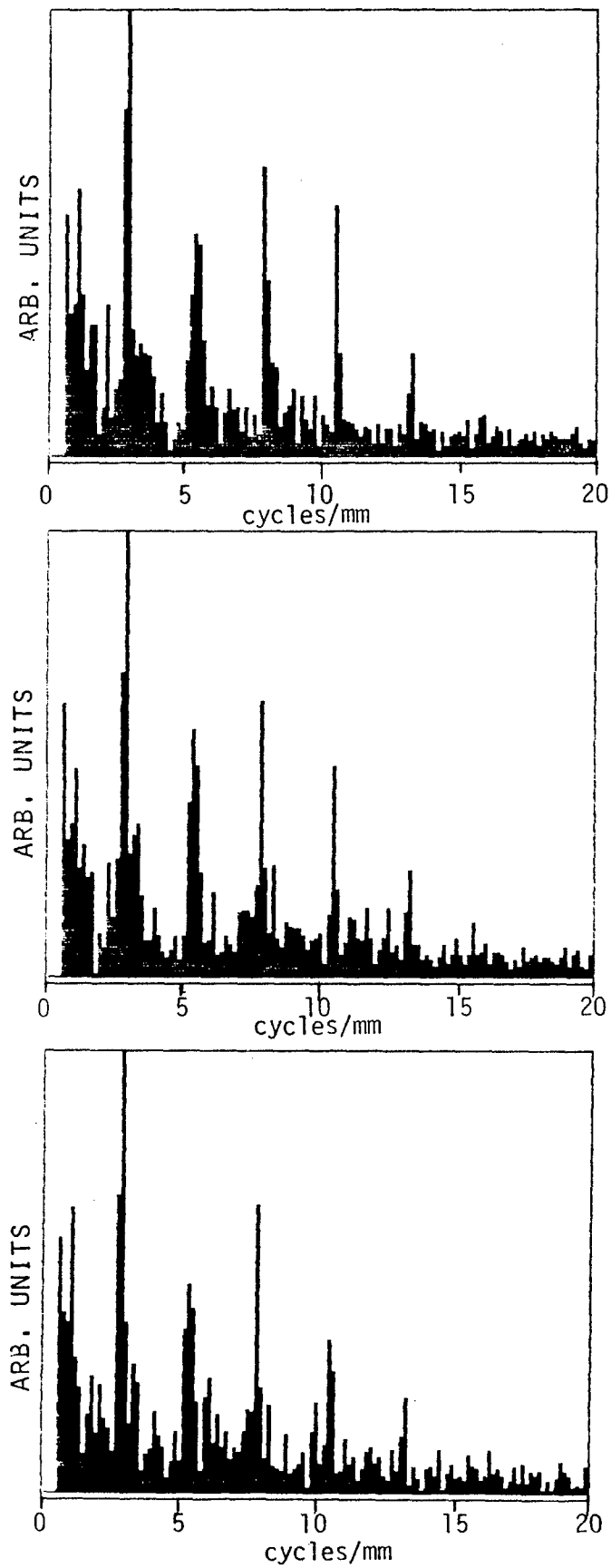

Fig. 13. Fourier transform power spectrum of three of the line scans for vertical milling standard N8 from Fig. 11.

5.0 DISPERSION IN RUBBER SAMPLES

5.1 **Rubber Sample Preparation.** Seven rubber samples were prepared by Mr. J. R. Beatty of Akron, Ohio for the study of dispersed particles in rubber. The rubber formulation was 100.0 parts polyisoprene and 2.5 parts dicumyl peroxide. Some samples include 40.0 parts high abrasion furnace black as the dispersed particles. Samples with smooth and rough surfaces were prepared. Smooth surfaces were obtained by curing the rubber in contact with a lithographic plate, while rough surfaces were prepared by curing the rubber in contact with a sand-blasted aluminum plate. Sample Type A is smooth, pure gum. Sample Type AB is smooth, with particles. Sample Type AR is rough, pure gum, while Type ABR is rough, with particles. One of the ABR samples has a light silicone spray on its surface. The size of the furnace black particles is smaller than the resolution obtained in these studies, so only inhomogeneities in the dispersion are likely to be thermally observable.

5.2 **Laser Beam Surface Damage.** A systematic study has been performed on these rubber samples to determine susceptibility to surface damage caused by laser beams used for thermal wave imaging. Earlier studies[12] recognized the possibility of localized damage to black rubber samples at powers as low as 5 mW, when combined with small focal spot size. Figure 14 shows the results of two-minute exposures to varying power levels, on Rubber Sample Type AB. The focal spot diameter was 100 μm (area = 7.85×10^{-9} m^2) for each exposure, and the exposed locations on the rubber sample are at equally spaced intervals. With the given combination of exposure time and focal spot size, damage is evident at power levels as low as 3mW. Power levels of 2.5 mW focused on the same area produce no appreciable damage during a typical scan for which the dwell time per point is about 0.1 sec.

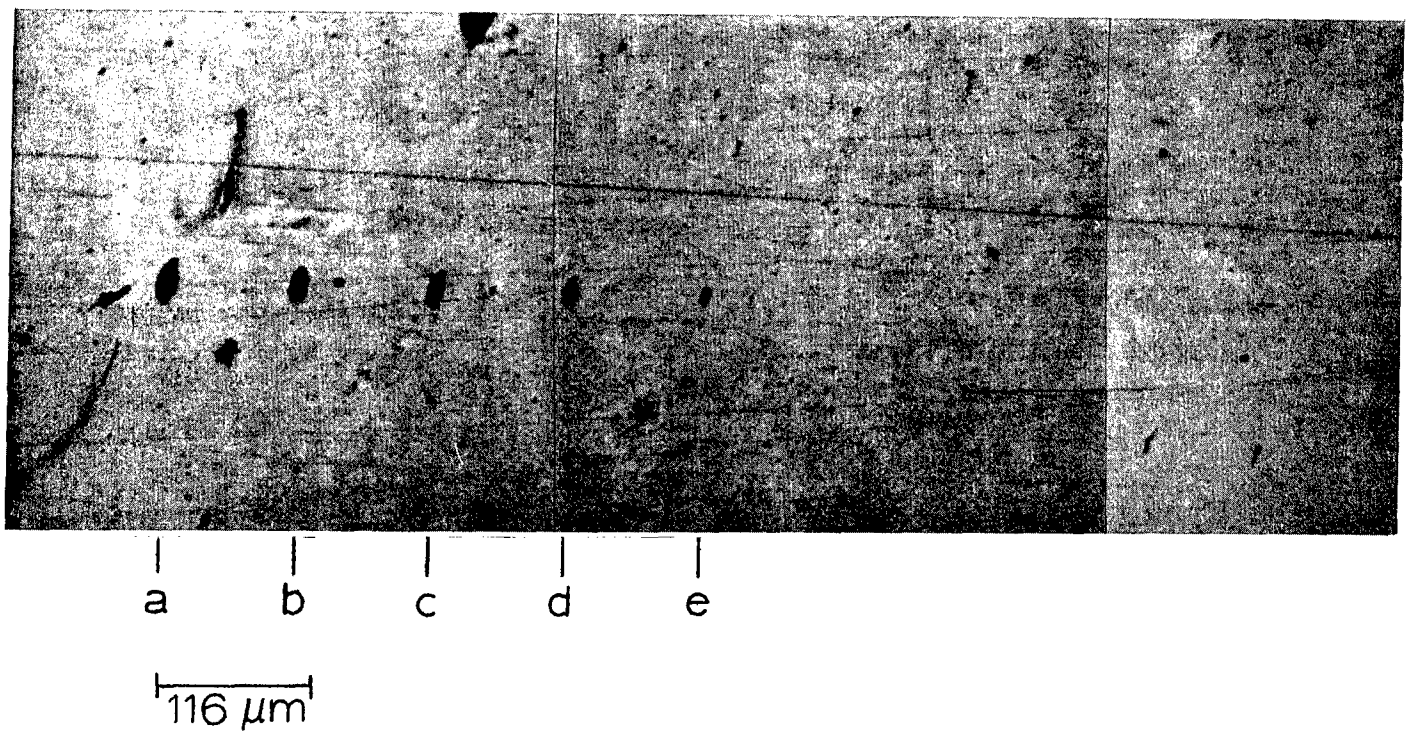

Fig. 14. Optical image of the surface of Rubber Sample AB following successive exposures of a range of Ar-ion laser power levels (a = 5 mW, b = 4.5 mW, c = 4.0 mW, d = 3.5 mW, e = 3.0 mW) for 2 minutes each at equally spaced intervals along a line on the sample. The area of the focal spot is approximately 8×10^{-9} m^2 (focal spot diameter 100 μm).

5.3 Thermal Wave Images. Representative thermal wave images are shown in Figs. 15-18. From these images one can conclude that much of the structure is related to surface condition. Note, for example, the difference between the images for the smooth (Fig. 17) and rough (Fig. 18) samples prepared from black loaded gum rubber. With the low thermal diffusivities for these samples, the two modulation frequencies (200 Hz and 400 Hz) used for acquiring data are perhaps too high to permit appreciable probing beneath the surfaces. The authors believe high abrasion furnace black is a poor choice for testing the ability of SPAM to detect subsurface dispersed particles. A more appropriate test defect should be selected before extending these studies to lower frequencies.

5.4 Optical Images. Optical images of the regions of the samples scanned thermally (see Figs. 15-18) are shown for comparison in Figs. 19 and 20.

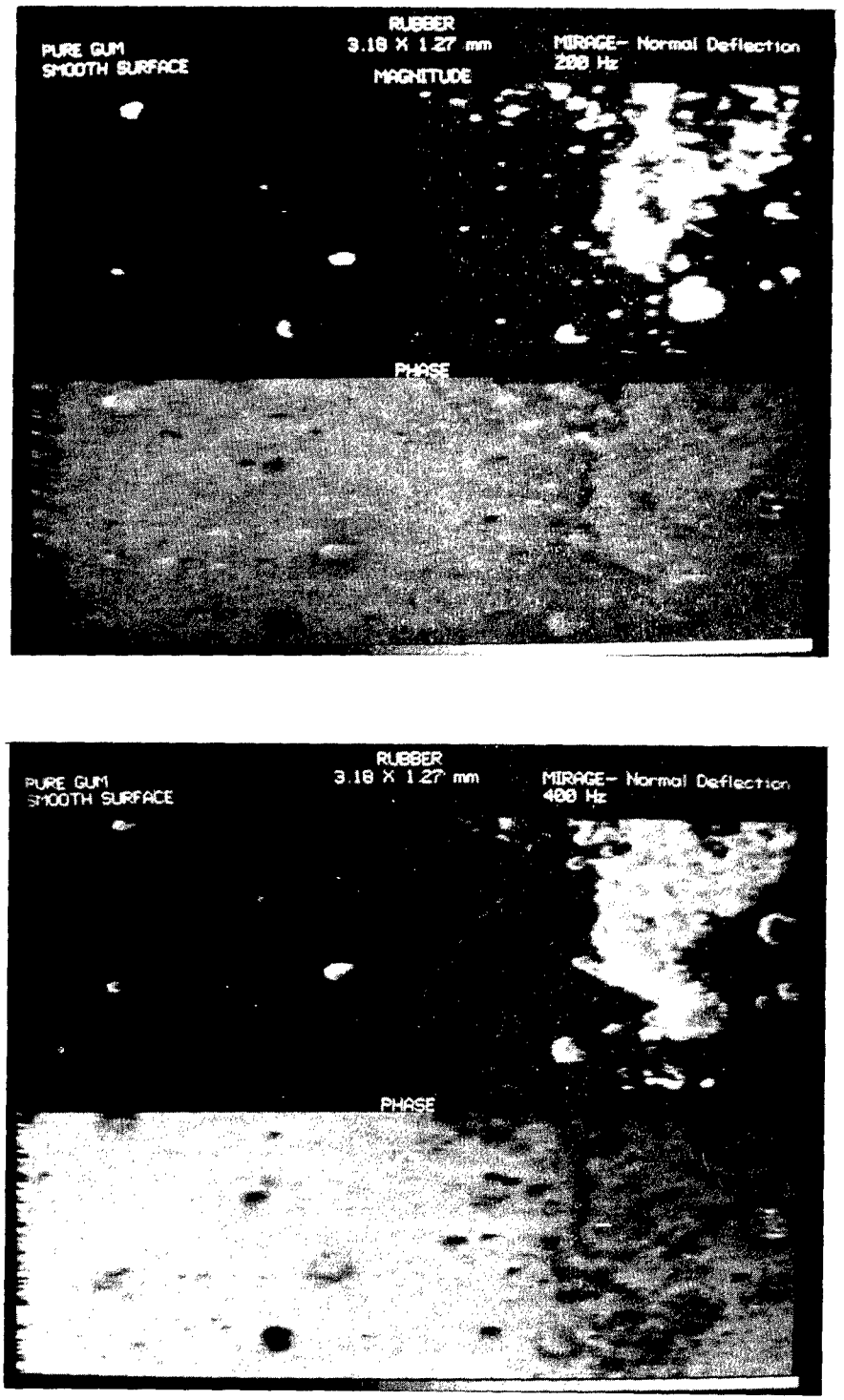

Fig. 15. Representative MIRAGE thermal wave images of Rubber Sample A (pure gum, smooth surface). [a) 200 Hz magnitude; b) 200 Hz phase; c) 400 Hz magnitude; d) 400 Hz phase].

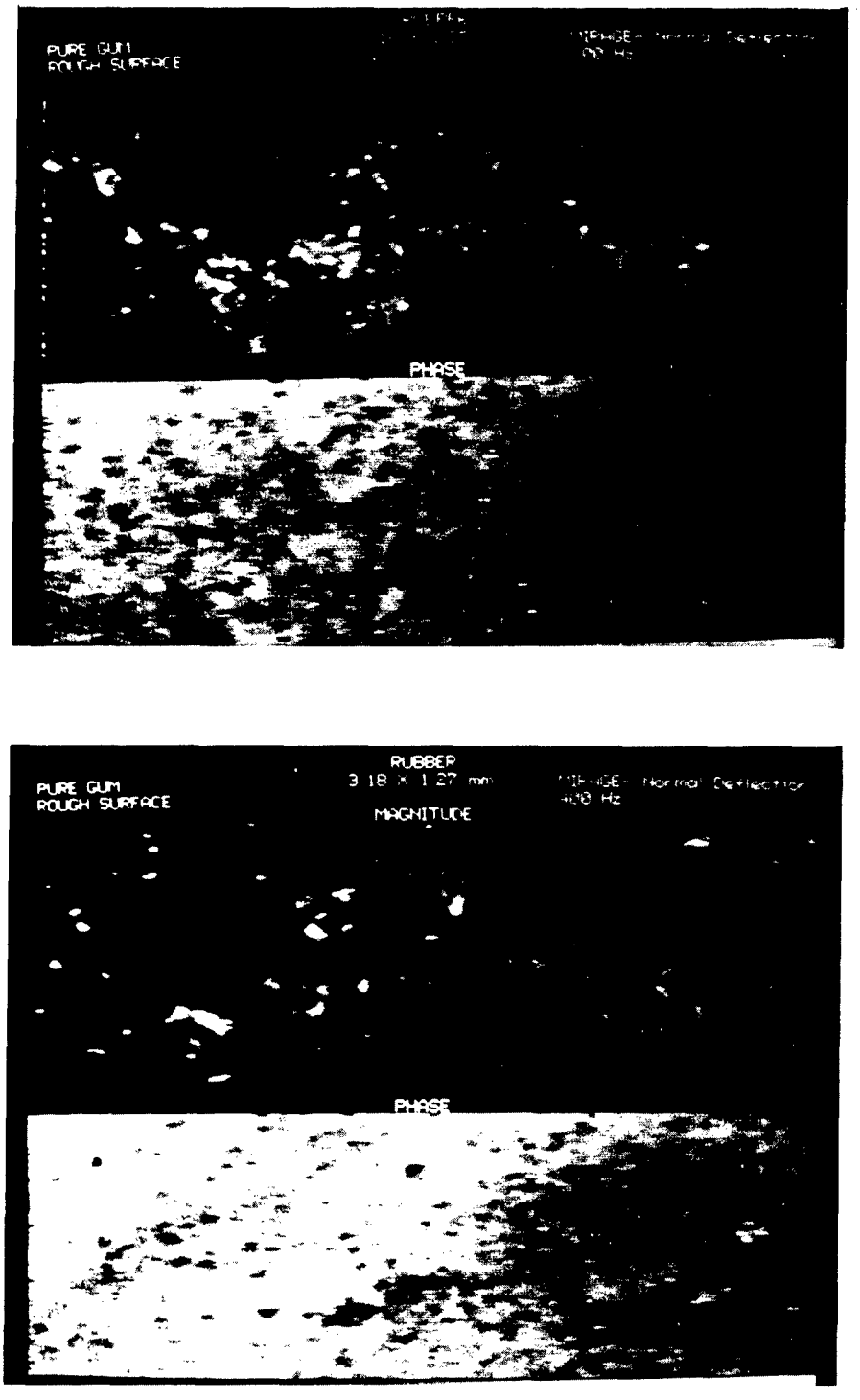

Fig. 16. Representative MIRAGE thermal wave images of Rubber Sample AR (pure gum, rough surface). [a) 200 Hz magnitude; b) 200 Hz phase; c) 400 Hz magnitude; d) 400 Hz phase].

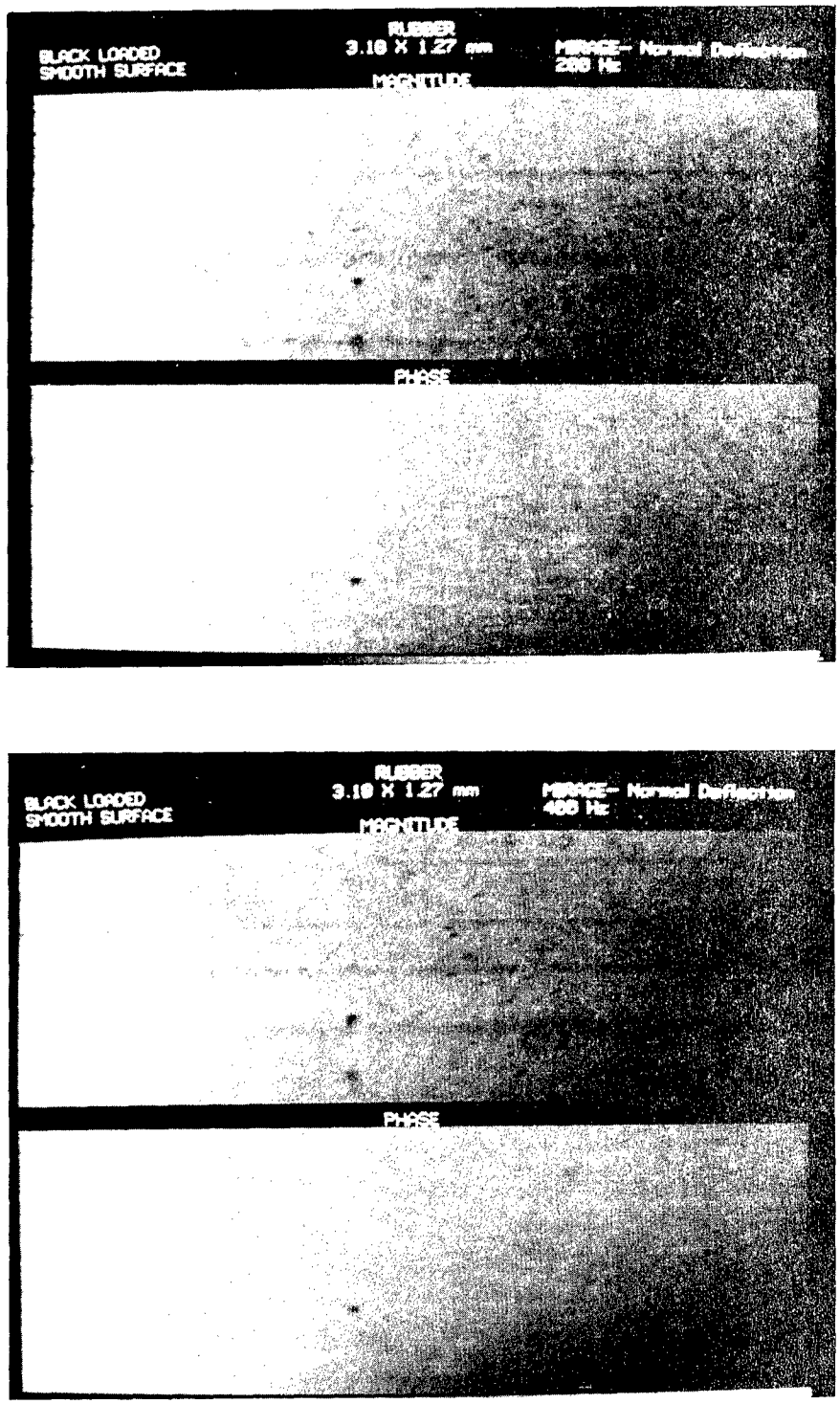

Fig. 17. Representative MIRAGE thermal wave images of Rubber Sample AB (black loaded, smooth surface). [a) 200 Hz magnitude; b) 200 Hz phase; c) 400 Hz magnitude; d) 400 Hz phase].

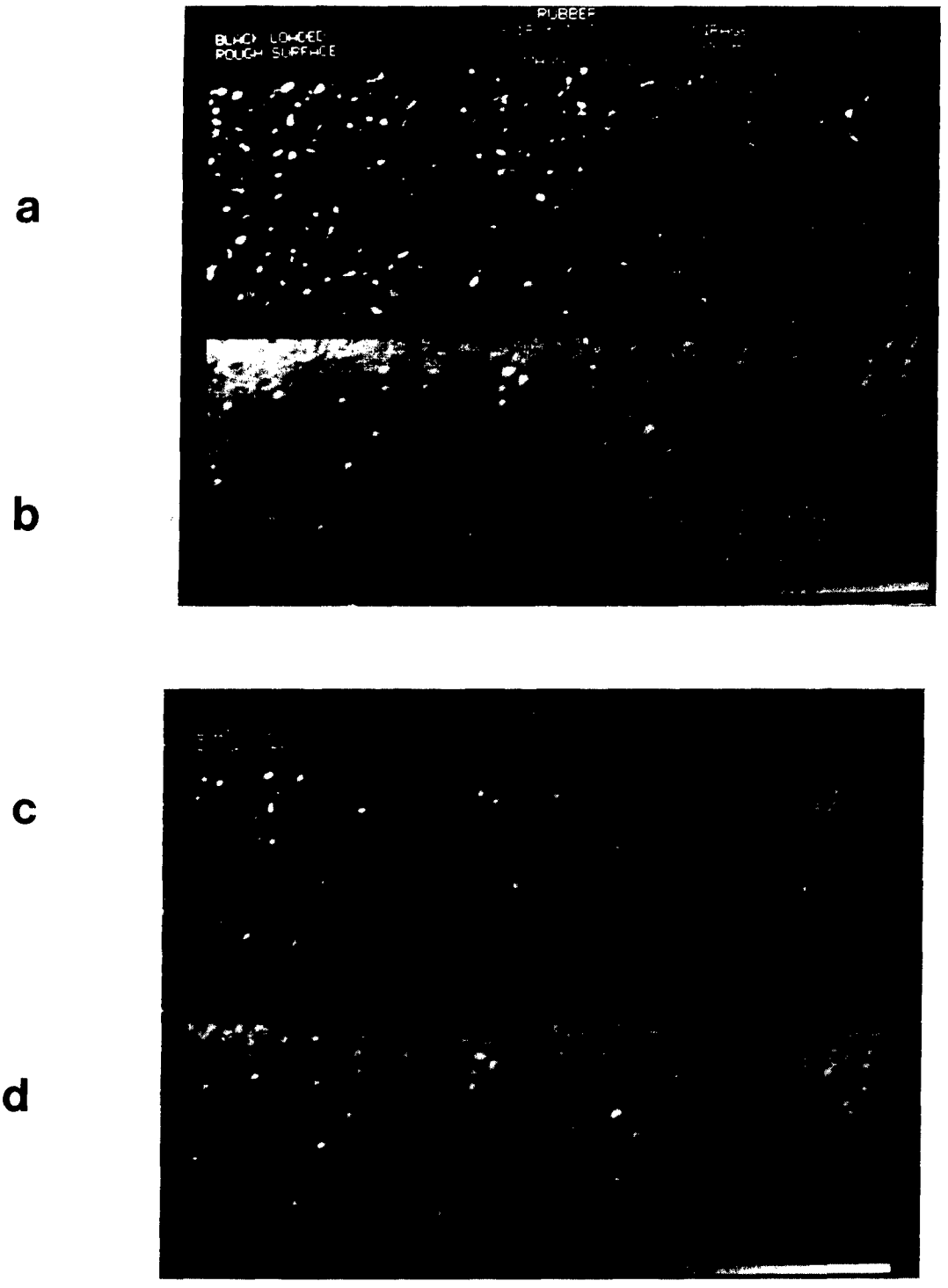

Fig. 18. Representative MIRAGE thermal wave images of Rubber Sample ABR (black loaded, rough surface). [a) 200 Hz magnitude; b) 200 Hz phase; c) 400 Hz magnitude; d) 400 Hz phase].

(a)

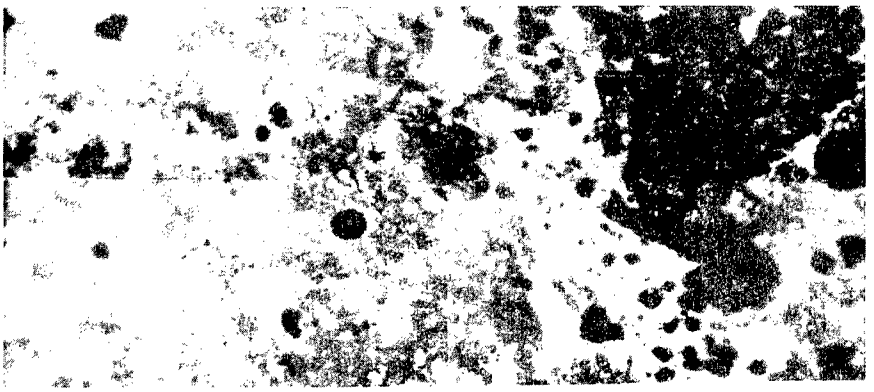

(b)

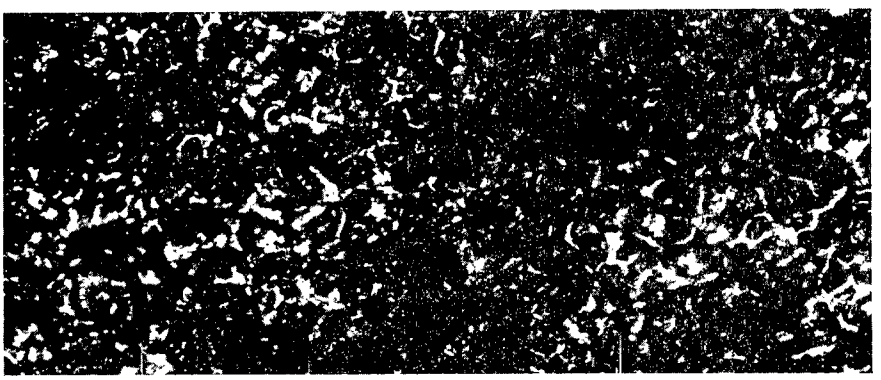

Fig. 19. Optical images of the regions of the pure gum rubber samples scanned thermally (see Figs. 15 and 16). a) Rubber Sample A (pure gum, smooth surface); b) Rubber Sample AR (pure gum, rough surface).

(a)

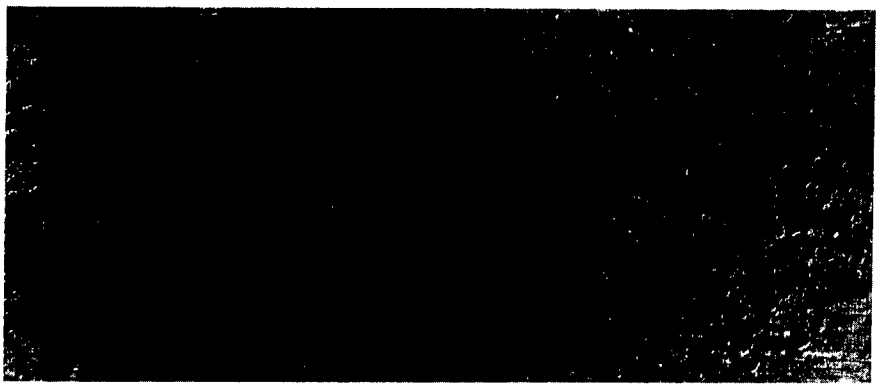

(b)

Fig. 20. Optical images of the regions of the black loaded rubber samples scanned thermally (see Figs. 17 and 18). a) Rubber Sample AB (black loaded, smooth surface); b) Rubber Sample ABR (black loaded, rough surface).

6.0 RECOMMENDATIONS

6.1 Color Encoding. The preliminary results of color-coding thermal wave images are encouraging. The authors recommend that further studies be made to develop the optimum pseudocolor parameters for selected classes of data. The feasibility of applying simple image processing routines should also be studied.

6.2 Coating Thickness Measurements. Neither SPAM nor MIRAGE thermal wave imaging was successful in assessing the coating uniformity of the CM 500 coated graphite samples. The authors recommend photothermal (infrared radiation) studies for these samples, as that technique samples the surface temperature variations directly, and has been successfully used by other workers[11] for similar problems.

6.3 Surface Roughness Measurements. More detailed study of numerical analysis methods is recommended for surface roughness data acquired by MIRAGE scanning. These methods include combining the spatial spectral content and the percentage variation of the thermal wave signal, and digital filtering. Studies should also be made to determine whether or not the percentage variation of the MIRAGE signal is independent of the height of the probe laser beam above the surface, as it must be to yield a reliable correlation with roughness.

6.4 Rubber Samples. It is recommended that optically opaque rubber samples be prepared with defects of at least 500 μm equivalent diameter, preferably of a high thermal conductivity substance (i.e., various metals), and located as close as possible to the surface (preferably closer than 100 μm). Such samples would allow systematic study of thermal wave propagation in rubber, including an estimate of the thermal diffusivity.

7.0 REFERENCES

1. Y.H. Wong, R.L. Thomas and G.F. Hawkins, Appl. Phys. Lett. 32, 538 (1978).
2. G. Busse, Appl. Phys. Lett. 35, 759 (1979).
3. J.J. Pouch, R.L. Thomas, Y.H. Wong, J. Schuldies, and J. Srinivasan, J. Opt. Soc. Am. 70, 562 (1980).
4. A. Rosencwaig, J. Appl. Phys. 51, 2210 (1980).
5. R.L. Thomas, J.J. Pouch, Y.H. Wong, L.D. Favro, P.K. Kuo, and A. Rosencwaig, J. Appl. Phys. 51, 1152 (1980).
6. L.D. Favro, P.K. Kuo, J.J. Pouch, and R.L. Thomas, Appl. Phys. Lett. 36, 953 (1980).
7. R.L. Thomas, L.D. Favro, L.J. Inglehart, P.K. Kuo, J. Lhota, and G. Busse, Proc. 1982 IEEE Ultrasonics Symposium, B. R. McAvoy, Ed., p.586.
8. L.D. Favro, P.K. Kuo, L.J. Inglehart, R.L. Thomas, and M. Srinivasan, J. Appl. Phys. 53, 1258 (1982).
9. K.R. Grice, L.J. Inglehart, L.D. Favro, P.K. Kuo, and R.L. Thomas, J. Appl. Phys. 54, 6245 (1983).
10. L.J. Inglehart, R.L. Thomas, and J. Schuldies, J. Nondes. Eval. 1, 287 (1980).
11. G. Busse, Appl. Opt. 21, 107 (1982).
12. R.L. Thomas, L.D. Favro, P.K. Kuo, and D.N. Rose, US Army Tank-Automotive Command Research and Development Center Technical Report No. 12668, July 1982.

Distribution List

	No. of Copies
Commander US Army Tank-Automotive Command ATTN: AMSTA-NS, Dr. H. H. Dobbs Technical Director, R&D Center Warren, MI 48090	1
Commander US Army Tank-Automotive Command ATTN: AMSTA-Z, Col. W. S. Chandler Acting Director, Tank-Automotive Concepts Laboratory Warren, MI 48090	1
Commander US Army Tank-Automotive Command ATTN: AMSTA-Z, Lt. Col. G. F. Rogers Deputy Director, Tank-Automotive Concepts Laboratory Warren, MI 48090	1
Commander US Army Tank-Automotive Command ATTN: AMSTA-Z S, Mr. D. W. Rees Chief, Survivability Research Division Warren, MI 48090	1
Director US Army Materials and Mechanics Research Center ATTN: AMXMR-EM, Mr. Perry R. Smoot Watertown, MA 02171 - 0001	1
Director US Army Materials and Mechanics Research Center ATTN: AMXMR-MI, Dr. Al Broz Watertown, MA 02171 - 0001	1

	No. of Copies
Director US Army Materials and Mechanics Research Center ATTN: AMXMR-S, Mr. Norm Fahey Watertown, MA 02172 - 0001	1
Commander US Army Research Office ATTN: Dr. George Mayer Director, Metallurgy and Materials Science Division P.O. Box 12211 Research Triangle Park, NC 27709	1
Commander US Army Research Office ATTN: Dr. Fred Schmeideshof P.O. Box 12211 Research Triangle Park, NC 27709	1
Commander Watervleit Arsenal ATTN: SARWV-QAE, Mr. Rick Campolini BLDG. 44 Watervleit,NY 12189	1
Commander Naval Coastal Systems Center ATTN: Code 715, Mr. Steve Gorin Panama City, FL 32407	1
Director Defense Advanced Research Projects Agency ATTN: Defense Sciences Office, Dr. E. Levinthal 1400 Wilson Boulevard Arlington, VA 22209	1
Deputy Director of Technology Defense Advanced Research Projects Agency ATTN: Mr. Lawrence Lynn 1400 Wilson Boulevard Arlington, VA 22209	1
Commander Harry Diamond Laboratories ATTN: DELHD-TD 2800 Powder Mill Road Adelphi, MD 20783	1

	No. of Copies
Commander US Army Mobility Equipment Research & Development Command ATTN: AMDME-WC (Tech Library) Fort Belvoir, VA 22060	1
Commander Defense Technical Information Center Cameron Station Alexandria, VA 22314	12
Superintendent US Naval Postgraduate School ATTN: Tech Rpts Sec Monterey, CA 93940	1
Director Naval Ships R&D Center ATTN: Code 1129, Mr. E. Wolfe Bethesda, MD 20084	1
Commander US Army Foreign Science & Technology Center ATTN: AMXST-CE Charlottesville, VA 29902	1
Commander US Army Missile Command ATTN: DRSMI-YM Redstone Arsenal, AL 35898	1
Dr. Robert P. Walson Cummins Engine Company, Inc. Mail Code 50165 Box 3005 Columbus, IN 47201	1
Mr. Alex Vary, Head Nondestructive Evaluation Section Materials DivisionMS 106-1 National Aeronautics and Space Administration Lewis Research Center 21000 Brookpark Road Cleveland, OH 44135	1
Commander US Army Tank-Automotive Command ATTN: AMSTA-ZSA, Mr. Zoltan Janosi Warren, MI 48090	1

	No. of Copies
Commander US Army Tank-Automotive Command ATTN: AMSTA-TSL Warren, MI 48090	2
Commander US Army Tank Automotive Command ATTN: AMSTA-RCKT, Mr. Jacob Patt Warren, MI 48090	1
Commander US Army Tank Automotive Command ATTN: AMSTA-QAT, Mr. Foster Brown Warren, MI 48090	2
Commander US Army Tank-Automotive Command ATTN: AMSTA-RSC, Mr. S. B. Catalano Warren, MI 48090	1
Commander US Army Tank-Automotive Command ATTN: AMSTA-RGET, Dr. Richard Munt Warren, MI 48090	1
Commander US Army Tank-Automotive Command ATTN: AMSTA-RGED, Dr. Walter Bryzik Warren, MI 48090	1
Commander US Army Tank-Automotive Command ATTN: AMSTA-RGET, Mr. John Lewakowski Warren, MI 48090	1
Commander US Army Tank-Automotive Command ATTN: AMSTA-TBM, Mr. W. A. Moncreif Warren, MI 48090	1
Director US Army Materials and Mechanics Research Center ATTN: AMXMR-CO, Dr. R. N. Katz Watertown, MA 02171 - 0001	1

	No. of Copies
Mr. Alan R. Hirasuma L'Garde, Inc 1555 Placentia Avenue Newport Beach, CA 92663	1
Dr. David Dwight 210 Holden Hall Materials Engineering Virginia Polytechnic Institute and State University Blacksburg, VA 24061	1
Mr. John M. Corwin Research Office Chrysler Corporation P.O. Box 1118 Detroit, MI 48288	1
Mr. John E. Becker STRBE-L US Army Belvoir Research & Development Center Ft. Belvoir, VA 22060	1
Dr. Harry Ringermacher United Technologies Research Center East Hartford, CT 06108	1
Prof. John Murphy Johns Hopkins Applied Physics Laboratory The Johns Hopkins University Johns Hopkins Road Laurel, MD 20810	1
Dr. Jacob Stiglich Aerojet General 2521 Michele Drive Tustin, CA 92680	1
Dr. James M. Toth Research Center Republic Steel Corp. 6801 Brecksville Rd. Cleveland, OH 44135	1

	No. of Copies
Dr. Ky Narasimham Spectra Research System Bldg. 860 Vandenburg AFB, CA 93437	1
Dr. Robert V. Ieth, Chief Scientist Div. 76 Hughes Aircraft P.O. Box 902 El Segundo, CA 90245	1
Dr. Thomas J. Moran AFWAL/MLLP Wright Patterson AFB, OH 45433	1
Dr. M. Srinivasan The Carborundum Company Advanced Materials Division P.O. Box 832 Niagara Falls, NY 14302	1
Dr. David W. Oliver General Electric Bldg. 37, Rm. 251 Schenectady, NY 12345	1
Dr. Vicki Panhuise Garrett Turbine Engine Company P.O. Box 5217 Phoenix, AZ 85010	1
Dr. Pramod Khandelwal Allison Gas Turbines P.O. Box 420, Mail Stop W-5 Indianapolis, Indiana 46206	1
Mr. Dennis Hornberger Sermetel, Inc. 155 South Limerick Rd. Limerick, PA 19468	1
Dr. Dale Chimente AFWAL/MLLP Wright Patterson AFB, OH 45433	1

	No. of Copies
Dr. Darryl P. Almond School of Materials Science University of Bath Cloverton Down Bath BA27AY Avon England	1
Mr. Ken Fizer Code 341 Naval Air Rework Facility Norfolk, VA 23511	1
Mr. George Lukes US Army Engineering Topographical Laboratory Research Institute Ft. Belvoir, VA 22060	1
Mr. Jim Kidd AMXMR-STM US Army Materials and Mechanics Research Center Watertown, MA 02172 - 0001	1
Dr. George Quinn AMXMR-MCP US Army Materials and Mechanics Research Center Watertown, MA 02172 - 0001	1
Dr. Tung-Ho Chen AMCCOM, ARDC EMD, Bldg. 3028 Dover, NJ 07801	1
Dr. Philip F. Kalina Central Research Inorganic Laboratory M.E. Pruitt Building (1776) Midland, MI 48460	1
Dr. Robert E. Singler AMXMR-OP US Army Materials and Mechanics Research Center Watertown, MA 02172 - 0001	1
Mr. Paul Doyle AMXMR-STM US Army Materials and Mechanics Research Center Watertown, MA 02172 - 0001	1

	No. of Copies
Dr. Dennis Viechniechi AMXMR-MCP US Army Materials and Mechanics Research Center Watertown, MA 02172 - 0001	1
Dr. Keith O. Legg School of Physics Georgia Technological University Atlanta, GA 30332	1
Mr. David M. Barrett Battelle Columbus Laboratories 505 King Avenue Columbus, OH 43201	1
Lt. Col. Ken Grice Dept. of Physics US Military Academy West Point, NY 10996	1
Mr. Al Frazer, Marketing Manager Electrooptical and Data System Group P.O. Box 902 El Segundo, CA 90245	1
Mr. Julius Frankel Benet Weapons Laboratory AMCCOM Bldg. 115 Watervliet, NY 12189	1
Mr. Henry Hartmann US Army AMCCOM (D) ATTN: B19, NDT Lab Dover, NJ 07801	1
Dr. Gary F. Hawkins Aerospace Corporation MS-M2-250 P.O. Box 92957 Los Angeles, CA 90009	1
Dr. Jim Lhota Aerospace Corporation MS-M2-250 P.O. Box 92957 Los Angeles, CA 90009	1

	No. of Copies
Dr. Arthur Tauber US Army Electronics Technology and Devices Laboratory DELET-ES Fort Monmouth, NJ 07703	1
Dr. M.H. Kamdar Large Caliber Weapons Laboratory AARADCOM, US Army Watervliet, NY 12189	1
Mr. Lewis J. Swank Ford Motor Co. Room E3172 SRL P.O. Box 2053 Dearborn, MI 48121	1
Mr. Michael DeLuca PCK Technology 322 L.I.E. Drive Melville, NY	1
Mr. John Zuccon Photoacoustics Laboratory Dept. of Mechanical Engineering University of Toronto Toronto, Ontario M55 1A4 CANADA	1
Dr. Christopher S. Berndt NASA-Lewis Research Center MS 105-1 2100 Brookpark Road Cleveland, OH 44135	1
Dr. Andrus Niiler AMDAR-BLF (A), Bldg. 120 Ballistic Research Laboratory Aberdeen Proving Ground, MD 21005	1
Dr. Wenzel E. Davidsohn AMXMR-OP US Army Materials and Mechanics Research Center Watertown, MA 02172 - 0001	1
Mr. Charles P. Gazzara AMXMR-OM US Army Materials and Mechanics Research Center Watertown, MA 02172 - 0001	1

	No. of Copies
Dr. James W. McCauley AMXMR-OP US Army Materials and Mechanics Research Center Watertown, MA 02172 - 0001	1
Dr. Robert W. McClung Oak Ridge National Laboratory 4500-S, D-61, Box X Oak Ridge, TN 37831	1
Dr. Janet S. Perkins AMXMR-OC US Army Materials and Mechanics Research Center Watertown, MA 02172 - 0001	1
Dr. Robert E. Richards 3M Company New Products Department 219-01-01, 3M Center St. Paul, MN 55144	1
Dr. Clay O. Ruud The Pennsylvania State University 159 Materials Research Laboratory University Park, PA 16802	1
Dr. Wayne K. Stuckey The Aerospace Corporation P.O. Box 92957, MS M2/250 Los Angeles, CA 90009	1
Dr. John B. Wachtman, Jr. Rutgers University Director, Center for Ceramics Research Room A274, P.O. Box 909 Piscataway, NJ 08854	1
Dr. James R. Wilshire Headquarters, Department of the Army Attn: DALO-PLO Rm. 2C-556 Washington, DC 20310	1
Mr. Fred Michel AMCMT US Army Material Command 5001 Eisenhower Avenue Alexandria, VA 22333	1

	No. of Copies
Mr. Mark Schumacher ATTN: M S971 Texas Instruments, Inc. 13500 N. Central Expressway Dallas, TX 75265	1
Mr. Walt Dudley Monsanto Research Corp Mound Lab Mound Road Miamisburg, OH 45342	1
Dr. Chuck Woods Monsanto Research Corp. Mound Lab Mound Road Miamisburg, OH 45342	1
Dr. Richard S. Quimby Physics Dept. Worcester Polytechnic Institute Worcester, MA 01609	1